Introduction to Mesh Based Generated Lumped Parameter Models for Electromagnetic Problems using Triangular Elements

Haidar Diab, Salim Asfirane, Nicolas Bracikowski, Frédéric Gillon, and Yacine Amara, *Senior Member, IEEE*

Abstract—This paper is an introduction to mesh based generated reluctance network modeling using triangular elements. Many contributions on mesh based generated reluctance networks using rectangular shaped elements have been published, but very few on those generated from a mesh using triangular elements. The use of triangular elements is aimed at extending the application of the approach to any shape of modeled devices. Basic concepts of the approach are presented in the case of electromagnetic devices. The procedure for coding the approach in the case of a flat linear permanent magnet machine is presented. Codes developed under MATLAB environment are also included.

Index Terms—Lumped parameter modeling, Finite element method, Mesh, Triangular elements, Electromagnetic devices, Modeling.

I. INTRODUCTION

THIS contribution is the continuity of the study presented in [1]. It aims at introduce the generation of reluctance network models using triangular elements. Indeed, while in [1], the mesh based generated reluctance networks (MBGRN) approach was introduced based on a uniform homogeneous mesh using rectangular elements Fig. 1(a), the goal in this contribution is to study the use of triangular elements Fig. 1(b). Many contributions on MBGRN using rectangular shaped elements have been published [1]–[7], but very few on those generated from a mesh using triangular elements [8]–[10].

The use of triangular elements, as for finite element method (FEM), allows modeling any shape of studied devices. Starting from the study presented in [1], the use of triangular reluctance elements is applied to the same flat linear permanent magnet machine, and to a second structure.

A pedagogical approach is adopted by comparing different

meshes schemes for the MBGRN. The results obtained from these models are compared to corresponding results issued from a FEM model (reference model). Interesting conclusions are then drawn. Since the aim is to study the use of triangular elements as compared to rectangular elements, the magnetic saturation is not considered (linear case).
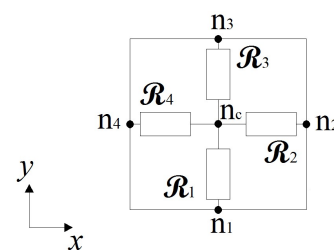
(a) Rectangular reluctance element
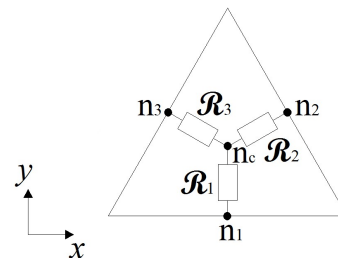
(b) Triangular reluctance element

Fig. 1. Elements used for the generation of the MBGRN models.

Nevertheless, since the mesh fluxes formulation (MFF) is superior to the magnetic scalar potential formulation (MSPF) [1] [11], when considering magnetic saturation, the approach is presented in the case of MFF. The MFF approach is also more convenient when considering electric current magnetic field sources. Codes developed under MATLAB environment are provided along this contribution

II. BASIC CONCEPTS OF THE MBGRN USING TRIANGULAR ELEMENTS

As mentioned in the "Introduction", the use of triangular elements is intended to allow the modeling of any shape of studied devices [12]. Indeed, rectangular shaped elements are not adapted for all geometric forms, and the simplest subdivision method consists of using triangular elements [12].

Aspects already discussed in contribution [1], and which are not dependent on the mesh elements shapes, i.e., mesh and elements numbering, boundary conditions consideration, and

motion consideration, are note discussed. Only aspects specific to the use of triangular reluctance elements are highlighted in following subsections.

In this contribution, as what was done in [1], for the sake of simplicity and in order to simply introduce the approach, it will be described in the case of a 2D problem (Cartesian coordinates) with a uniform homogeneous mesh. This will also ease the programming aspect. By doing so, geometric and physics properties may not be perfectly respected, and this will have an impact on the results quality as will be seen in following section when studying the illustrative example.

A. Triangular Reluctance Elements

The computation of the three reluctances (or permeances) composing the triangular reluctance element is presented in this subsection.

Fig. 2 illustrates how this is done for one side (side 1) of the triangular element. Knowing the coordinates of the three triangle vertices Fig. 2(a), the coordinates of the centroid point (or node) (barycenter) is first defined Fig. 2(b):

$$\begin{cases} x_{n_c} = \dfrac{x_1 + x_2 + x_3}{3} \\ y_{n_c} = \dfrac{y_1 + y_2 + y_3}{3} \end{cases} \tag{1}$$

The expression of the reluctance joining the middle of the side (side 1) "n_1" to the central node "n_c" is given by Fig. 2(c) [13]:

$$\mathcal{R}_1 = \frac{1}{\mu_0 \mu_r} \frac{h \ln(w_2/w_1)}{l_a (w_2 - w_1)} \tag{2}$$

where h, w_1 and w_2 are defined in Fig. 2(d), μ_0 and μ_r are the permeability of the vacuum and the relative permeability of the region (material) where the element is located, and finally, l_a is the active length of modeled problem. It corresponds to the reluctance of a trapezoidal element when the flux tube is crossing from one base to another perpendicularly [13].

(a) Vertices of the triangle   (b) Centroid of the triangle

(c) Reluctance of the trapezoidal   (d) Trapezoidal sub-element
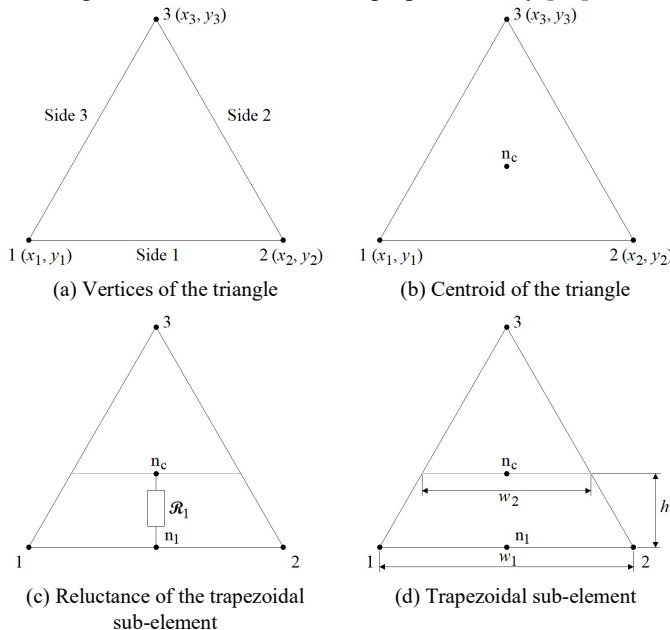   sub-element

Fig. 2. Illustration of reluctances computation for a triangular element.

The expressions of the reluctances for the two other sides are determined similarly. More details are provided in the Appendix.

The trapezoid parallels are the line supporting "Side 1", and the line passing by the centroid "n_c". The lines supporting the legs are those supporting the two other sides of the triangle element, i.e., "Side 2" and "Side 3".

In the following subsection, the way the magnetic field sources are modeled is presented. It is more particularly the modeling of permanent magnets (PM) field sources which is discussed.

B. Magnetic Field Sources Modeling

Since MFF (Mesh Fluxes Formulation) is adopted, the consideration of magnetic field sources due to coils or windings is naturally done through the Ampere's law [1]. Permanent magnets (PM) magnetic field sources are oriented field sources and can have different shapes (Fig. 3). Fig. 3 shows, as an example, two cylindrical shaped PMs with two different remanence magnetizations. The general rule to follow when modeling PM field sources in MBGRN is to use reluctance elements which respect, whenever possible, both the shape of the PM and its remanence magnetization orientation.

Permanent magnets can either be modeled by a flux source in parallel with a reluctance or a magneto-motive force MMF in series with a reluctance, as shown in Fig. 4 [1]. B_r is the remanence induction. In the rest of this contribution, it is the second option which is adopted.

Fig. 5 shows a simple magnetic circuit including a PM ($B_r = 1.2$ T and $\mu_{rpm} = 1$). It is used in order to illustrate the approach adopted for the modeling of PM magnetic field sources using triangular reluctance elements, and the effect of not perfectly following the previously stated rule.
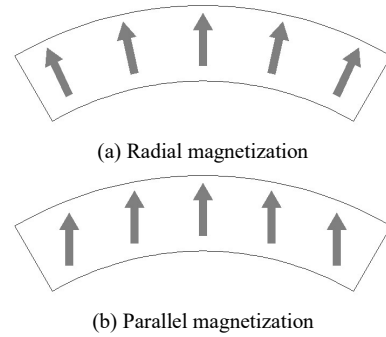

(a) Radial magnetization

(b) Parallel magnetization

Fig. 3. Permanent magnets with radial and parallel magnetization pattern.

$$\begin{cases} \mathcal{R}_{pm} = \dfrac{1}{\mu_0 \mu_{rpm}} \dfrac{h}{l_a w} \\ \Phi_{pm} = B_r l w \\ F_{pm} = \dfrac{B_r}{\mu_0 \mu_{rpm}} h \end{cases}$$

Fig. 4. Permanent magnet (PM) region modeling.

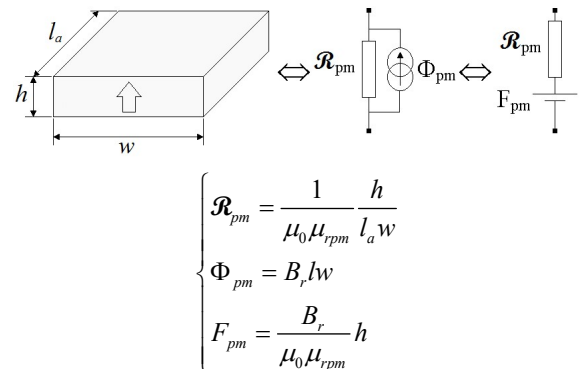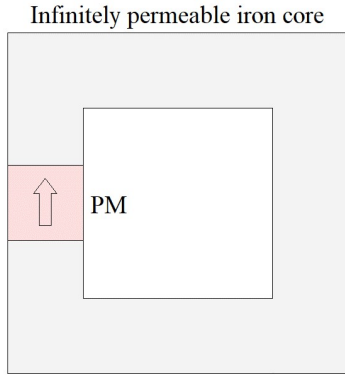Infinitely permeable iron core

Fig. 5. Magnetic circuit including a PM.

In this example, the PM cross section is a perfect square of 5 cm side. Tangential magnetic field boundary condition is applied at inner and outer surfaces of this magnetic circuit. Considering the PM shape, it is first modeled using a rectangular (square) element Fig. 6(a), and then using two triangular elements Fig. 6(b).

Each branch of the reluctance elements modeling the PM is constituted of a reluctance in series with a magneto-motive force (MMF) source F_{pm} Fig. 6(c). The computation of the MMF value is explained for the branch connected to the third side of the triangular reluctance element shown in Fig. 7(a).
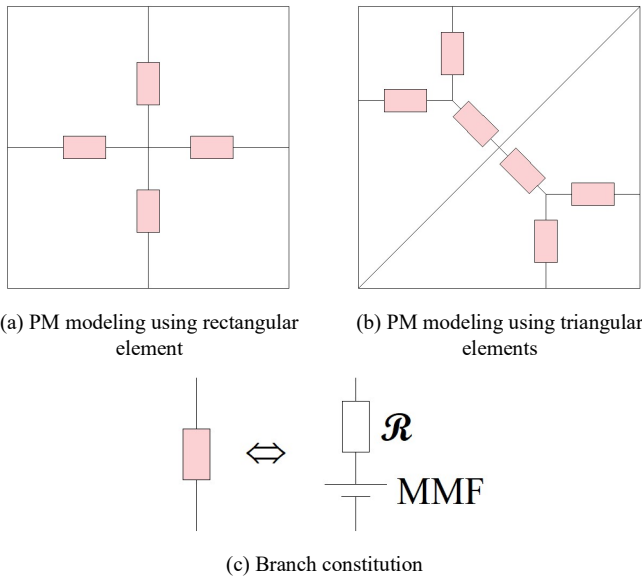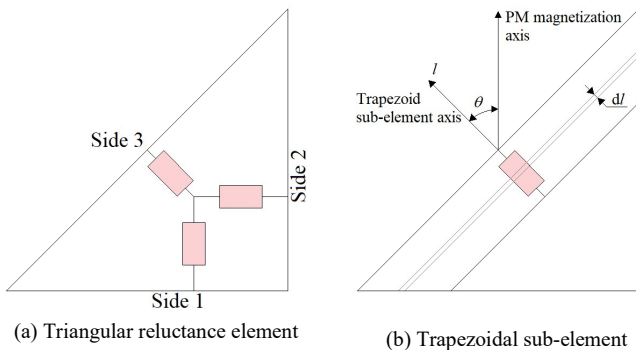

(a) PM modeling using rectangular element

(b) PM modeling using triangular elements

(c) Branch constitution

Fig. 6. PM modeling using different reluctance elements types.

(a) Triangular reluctance element

(b) Trapezoidal sub-element

Fig. 7. Computation of MMF sources F_{pm} for a triangular element branch.

In previous sub-section, it has been indicated that the reluctance in a triangular reluctance element is joining the middle of a side to the centroid node; this is not rigorously true, since the reluctance is computed considering the line perpendicular to the trapezoid sub-element bases and passing through the centroid node (centroid point of the triangle) Fig. 7(b). It is referred to this line as the trapezoid sub-element axis in Fig. 7(b). This line may not necessarily intersect the triangle side (larger base of the trapezoid sub-element) at its middle. This is why in Figs. 6 and 7 the branches are drawn following these axes. Representing these branches by joining the middle of the elements sides to the centroid nodes help simplify the RN representation, since two triangular reluctance elements share an edge (or a side).

Considering this trapezoid sub-element isolated in a magnetic circuit with an infinitely permeable iron core, with no current source, the application of Ampere's law states that

$$\oint \vec{H}_{pm}\ \vec{dl} = 0 , \qquad (3)$$

and considering the PM characteristic

$$\vec{B}_{pm} = \vec{B}_r + \mu_{rpm}\mu_0 \vec{H}_{pm} , \qquad (4)$$

it can be established that

$$\int_0^h \vec{B}_{pm}\ \vec{dl} - B_r h \cos\theta = 0 , \qquad (5)$$

where h is the trapezoid sub-element height, and θ is the angle between the PM magnetization axis and the trapezoid axis Fig. 7(b).

Considering the assumption that the trapezoid sub-element is a flux tube where the flux density vector is collinear to the trapezoid axis Fig. 7(b), equation (5) can be rewritten as follows

$$\int_0^h \frac{\Phi_{pm}}{\left(w_1 + \frac{(w_2 - w_1)}{h} l \right) l_a} dl - B_r h \cos\theta = 0 , \qquad (6)$$

where w_1 and w_2 are the trapezoid bases lengths.

Knowing that the magnetic flux is constant throughout the flux tube and that it is given by

$$\Phi_{pm} = \frac{F_{pm}}{\mathcal{R}_{pm}} , \qquad (7)$$

the PM MMF source F_{pm} related to the trapezoidal sub-element is then given by

$$F_{pm} = \Phi_{pm}\mathcal{R}_{pm} = = \frac{B_r h \cos(\theta)}{\mu_0 \mu_{rpm}} . \qquad (8)$$

Following the same developments, the PM MMF sources F_{pm} for the other branches, whether for triangular reluctance elements or rectangular ones, can be determined.

The magnetic circuit presented at Fig. 5 has then been simulated using FEM, and the two reluctance network (RN) models obtained from the two meshes presented by Fig. 6. While the FEM and the RN model issued from the rectangular element Fig. 6(a) give an average magnetic flux density amplitude of ≈ 1.2 T in the magnetic circuit, this value drops to

≈ 0.99 T for the RN model issued from the triangular elements mesh Fig. 6(b), which means an absolute value of relative error of about 17 %.

This error is mainly due to the fact that the use of triangular elements, to model the square shape PM, forces the orientation of the magnetic flux of the PM in a direction which is unnatural regarding its magnetization vector.

This effect will also be noticeable when studying the illustrative example with different meshes schemes.

III. ILLUSTRATIVE EXAMPLES

In order to illustrate the use of adopted triangular elements, two examples are presented.

A. First Example

The flat linear permanent magnet machine (FLPM) (Fig. 8) used as an illustrating example in reference [1], is used again to study the use of triangular reluctance elements. Table I recalls main machine's dimensions.

Along with a FEM model, six meshes schemes for the MBGRN are used for studying different aspects related to the approach. The six schemes are as follows (Fig. 9):

1) MBGRN generated from a homogenous regular mesh using rectangular (square) reluctance elements [1];

2) MBGRN generated from a homogenous regular mesh using triangular elements (Fig. 10);

3) MBGRN generated from a homogenous regular mesh using rectangular (square) elements for the mobile armature and the air-gap, and triangular elements for the stator part (stator iron core and the slots);

4) MBGRN generated from a homogenous regular mesh using triangular elements for the mobile armature and the air-gap, and rectangular (square) elements for the stator part (stator iron core and the slots);

5) MBGRN generated from a homogenous regular mesh using rectangular (square) elements for the mobile armature and half the air-gap, and triangular elements for the stator part (the second half of the air-gap, stator iron core and the slots);

6) MBGRN generated from a homogenous regular mesh using triangular elements for the mobile armature and half the air-gap, and rectangular (square) elements for the stator part (the second half of the air-gap, stator iron core and the slots).
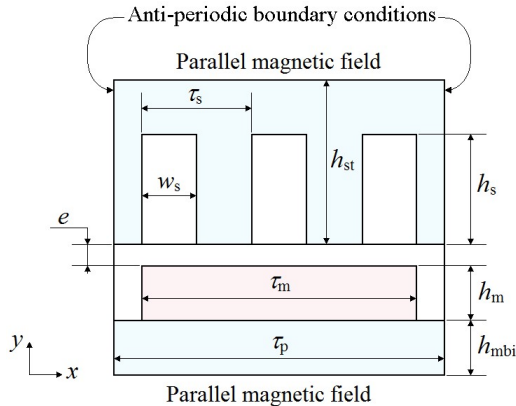

Fig. 8. Longitudinal cross-sectional vie of the studied FLPM structure.

TABLE I
MACHINE CHARACTERISTCS

Mechanical air-gap e (mm)	1
Pole pitch τ_p (mm)	60
h_{st}, h_s, h_m, h_{mbi}, τ_m, τ_s and w_s (mm)	30, 20, 10, 10, 55, 20, 10
Active length (mm)	1000
PM magnetic remanence B_r (T)	1.2
Relative permeability of iron μ_{rf} and PM μ_{rpm}	7500, 1

(a) Mesh scheme M1   (b) Mesh scheme M2

(c) Mesh scheme M3   (d) Mesh scheme M4

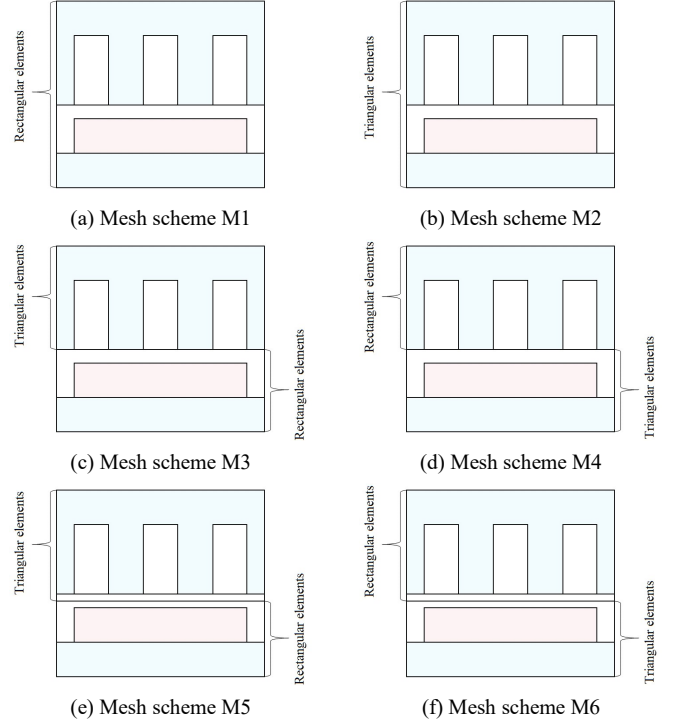(e) Mesh scheme M5   (f) Mesh scheme M6

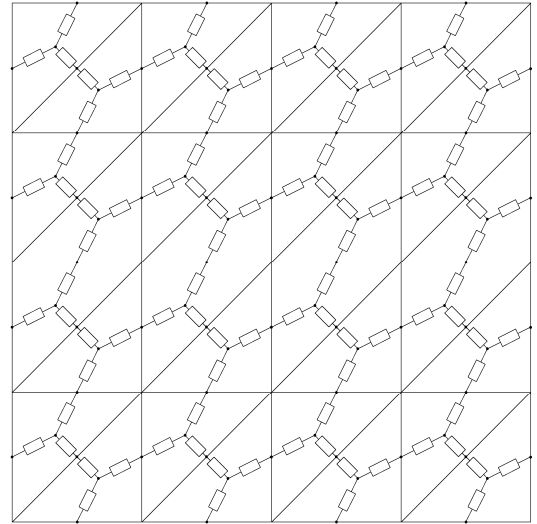Fig. 9. The different MBGRN meshes schemes.

Fig. 10. Homogenous regular mesh using triangular reluctance elements.

Fig. 10 shows the homogenous regular mesh based on triangular reluctance elements. This mesh is obtained by dividing the rectangular elements adopted in reference [1] into two triangular elements as illustrated by Fig. 11. As compared to the mesh scheme adopted in [1], the same mesh fluxes number is obtained for the MFF, but each mesh is connected to 6 adjacent meshes, instead of 4 for the rectangular elements.
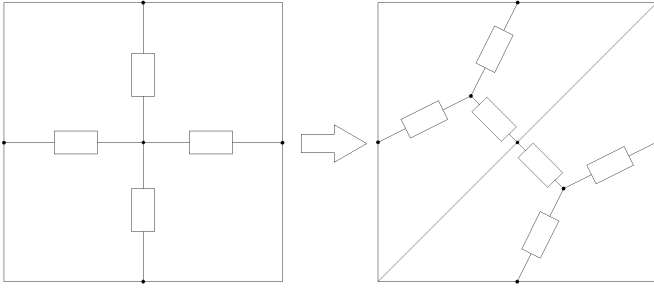
Fig. 11. Triangular elements mesh scheme obtained from the rectangular mesh scheme.

Due to geometric and electromagnetic symmetries; only one pole pitch is modeled. Anti-periodic boundary conditions are adopted. Table I gives main machine's dimensions. Adopted boundary conditions are shown in Fig. 8.

Programs coded under MATLAB environment allowing the analyses can be downloaded from [14]. They are coded using simple instructions.

1) Computation of Local Quantities

The magnetic field **B** components at the central node of a triangular element (Fig. 12) are computed by

$$\begin{cases} B_x = \dfrac{\mu_r\mu_0}{(S_{T2}+S_{T3})}\cdot\left(S_{T2}\dfrac{\mathcal{R}_2\Phi_2}{h_{T2}}-S_{T3}\dfrac{\mathcal{R}_3\Phi_3}{h_{T3}}\sin(\theta)\right) \\ B_y = \dfrac{\mu_r\mu_0}{(S_{T1}+S_{T3})}\cdot\left(S_{T1}\dfrac{\mathcal{R}_1\Phi_1}{h_{T1}}+S_{T3}\dfrac{\mathcal{R}_3\Phi_3}{h_{T3}}\cos(\theta)\right) \end{cases}. (9)$$

Fig. 12 shows some of the quantities used in (9). S_{T1}, S_{T2}, S_{T3}, and h_{T1}, h_{T2}, h_{T3} correspond to surface areas and heights of the three trapezoidal sub-elements of the triangular elements, respectively. The magnetic field components computation in the case of a rectangular element has been described in [1].

The local quantities are used to compute global quantities. The global quantities are computed the same way as described in [1].

2) Comparison with FEM

FLUX2D package [15] is used for the FEM computations. The number of unknowns for all MBGRN meshes schemes is equal to 12120 mesh fluxes. In all meshes schemes, the air-gap contains two layers of elements. It is referred to results from the MBGRN in following figures by simply using the acronym RN, to which a reference to the mesh scheme is added.
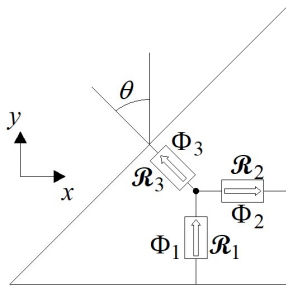

Fig. 12. Computation of magnetic field **B** components for the central node of a triangular element.

The first mesh scheme M1 was the subject of reference [1]. It was based on square reluctance elements, which corresponds to

the natural mesh scheme for the studied example, considering the geometric and physical properties of the structure and the different magnetic field sources. This mesh scheme gave results which were in very good agreement with those obtained from FEM.

Fig. 13 compares magnetic field **B** components under open-circuit condition for the second mesh scheme M2. The position for which these spatial distributions are plotted corresponds to the one of Fig. 8, the PM having a positive magnetization. The origin point ($x = 0$ m, $y = 0$ m) corresponds to the bottom-left corner of the structure. The spatial distributions are plotted for a path located at $y = h_{mbi} + h_m + 3e/4$. A noticeable discrepancy does exist between the RN M2 results and those issued from the FEM. Fig. 14 compares the phase electromotive force (EMF) per turn, for one pole pair, for a linear speed $v = 1$ m/s. Again, a noticeable discrepancy is visible. The absolute value of relative error of RMS values of EMF waveforms obtained from both approaches, i.e., FEM and RN M2, computed as ($|\text{EMF}_{\text{FEM RMS}} - \text{EMF}_{\text{RN M2 RMS}}| / \text{EMF}_{\text{FEM RMS}}$), is about 18 %.

Fig. 15(a) compares magnetic field **B** components only due to armature reaction field (ARF) (no PM). Fig. 15(b) shows in which conditions these spatial distributions are obtained.

It can be seen that even if the discrepancy is not as important as in Fig. 13, it is still significant.
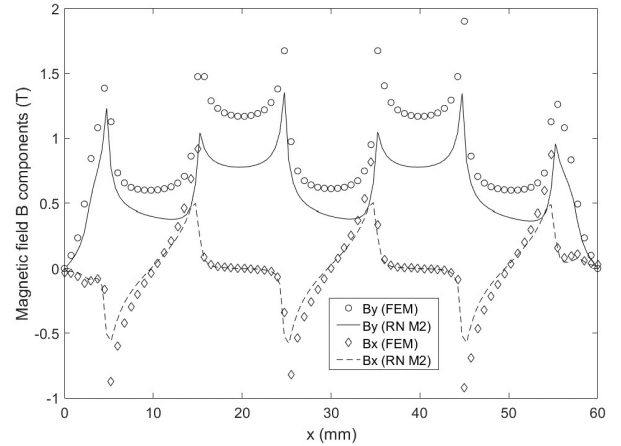

Fig. 13. Magnetic field B components in the air-gap (open-circuit condition).
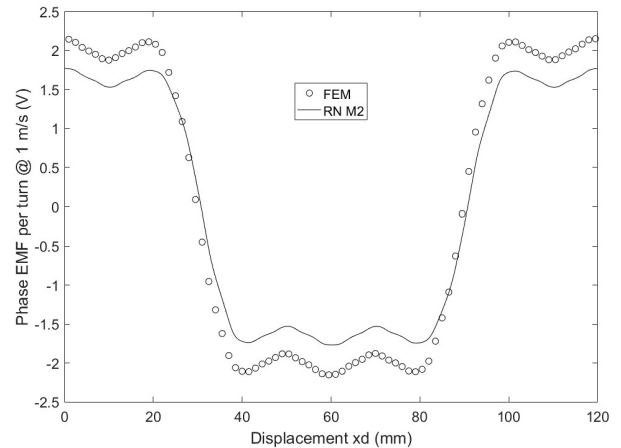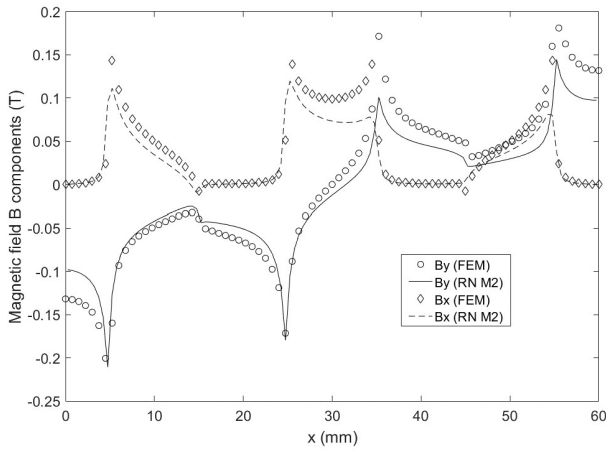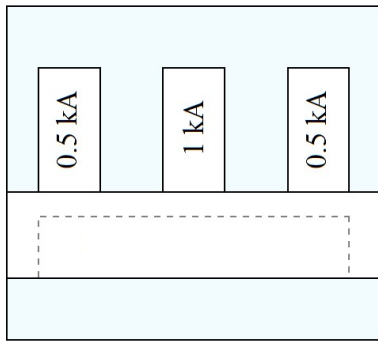

Fig. 14. Comparison of EMF waveforms for a linear speed $v = 1$ m/s.

(a) Magnetic field B components in the air-gap (armature field reaction).

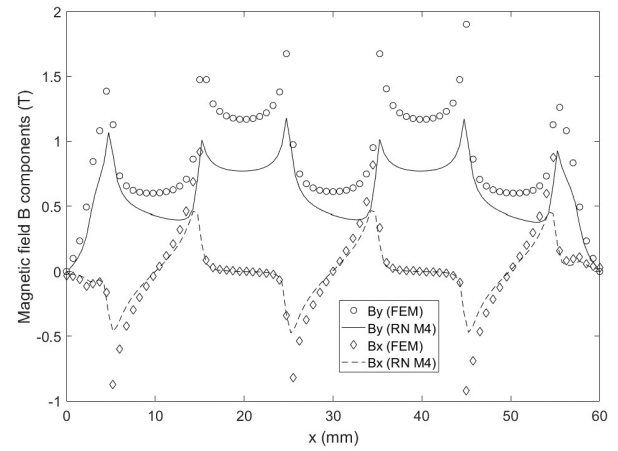(b) Illustration of the conditions of computation of the ARF.

Fig. 15. Comparison of ARF magnetic field components.

(a) Magnetic field B components in the air-gap (open-circuit condition)

(b) EMF waveforms for a linear speed v = 1 m/s

Fig. 16. Comparison open circuit quantities obtained from FEM and RN M4.

Figs. 16 and 17 compare the open circuit magnetic field **B** components, and the EMF waveforms for meshes schemes M4 and M6, respectively. As for the mesh scheme M2, the discrepancy is significant. The absolute value of relative error of RMS values of EMF waveforms, obtained from the two meshes schemes M4 and M6, as compared to the waveform obtained from the FEM is about 17 %. The magnetic field **B** components obtained from RN M6 Fig. 17(a) look better, as compared to FEM waveforms, than those obtained from RN M4 Fig. 16(a). This is mainly due to the fact that the computation of these components waveforms involves fewer approximations for the RN M6 as compared to RN M4. Indeed, for RN M6 the half air-gap where these components are computed is meshed using rectangular elements, while it is meshed using triangular elements for RN M4 (Fig. 9).
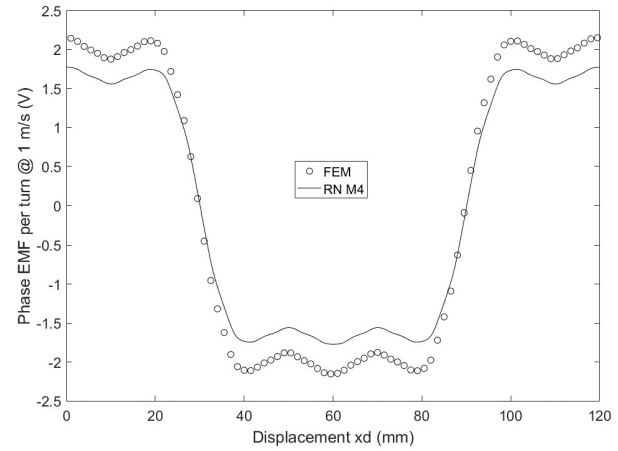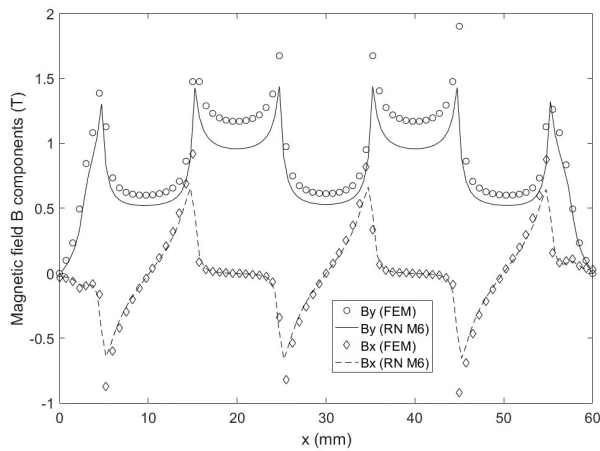
Meshes schemes M2, M4 and M6 share the fact that the PM region is meshed using triangular reluctance elements which is not a natural choice, considering the geometric (rectangular section) and physics (a remanence magnetization in y direction) properties of this region.

Figs. 18 and 19 compare the magnetic field **B** components under open-circuit condition for the meshes schemes M3 and M5. It can be seen that while a good agreement is obtained for the RN M3, a noticeable discrepancy does exist between the RN M5 results and those issued from the FEM.

For both meshes schemes M3 and M5, the PM region is meshed using rectangular (square) elements (Fig. 9).

For the RN M5 the discrepancy is persistent, although the PM region is meshed using rectangular (square) elements. This is mainly due to the way the components are computed. Indeed, Fig. 20 is comparing same components for the RN M5 model, for a path located at $y = h_{mbi} + h_m + e/4$, and in this case a fairly good agreement is obtained. This path is located in an element layer only constituted of rectangular elements, where the components computation is requiring fewer approximations as compared to the case involving triangular elements. Considering this fact, the computation of magnetic field **B** components, used along the Maxwell's stress method in order to estimate the forces using the RN M5 model, is done for a path located at $y = h_{mbi} + h_m + e/4$.
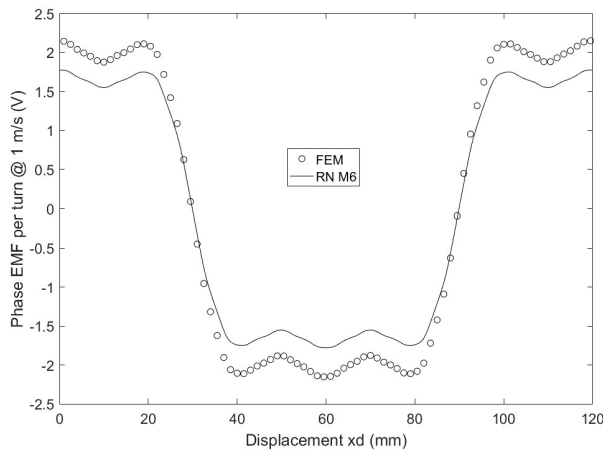
Fig. 21 compares the EMF waveforms obtained from the FEM and the RN M3. Figs. 22(a) and 22(b) compare the cogging force and the thrust force, respectively. For the thrust force estimation, the current in each phase is imposed with a null phase shift with the corresponding phase EMF (Maximum force per-Ampere (MFPA) control). The maximum current density is set equal to 5 A/mm^2. As can be seen a good agreements is obtained.

Figs. 23 and 24 compare corresponding quantities obtained from the FEM and the RN M5.

It can be seen that the global quantities computed from RN M3 and RN M5 are in fairly good agreement with these

DIAB et al : INTRODUCTION TO MESH BASED GENERATED LUMPED PARAMETER MODELS FOR ELECTROMAGNETIC PROBLEMS USING TRIANGULAR ELEMENTS

27

(a) Magnetic field B components in the air-gap (open-circuit condition)

(b) EMF waveforms for a linear speed $v = 1$ m/s

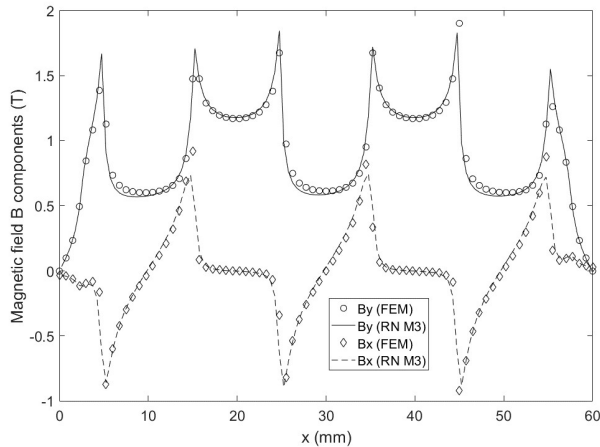Fig. 17. Comparison open circuit quantities obtained from FEM and RN M6.

Fig. 18. Comparison of magnetic field B components in the air-gap (open-circuit condition) obtained from FEM and RN M3.
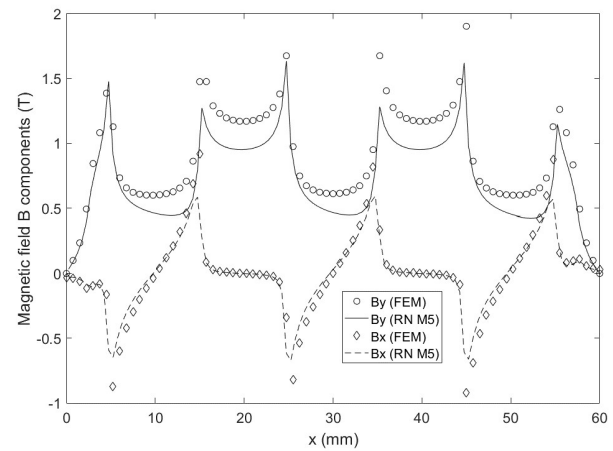

Fig. 19. Comparison of magnetic field B components in the air-gap (open-circuit condition) obtained from FEM and RN M5 ($y = h_{mbi} + h_m + 3e/4$).
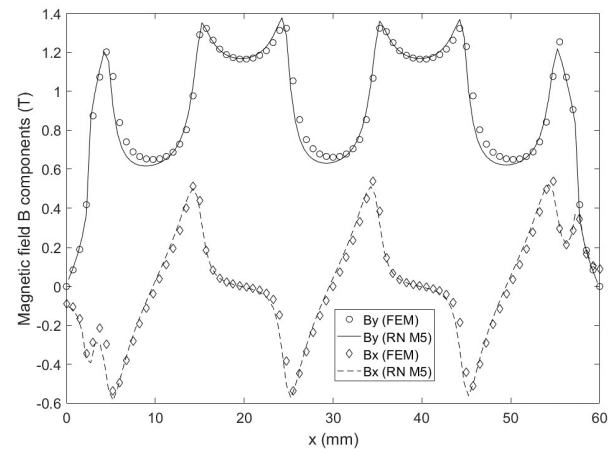

Fig. 20. Comparison of magnetic field B components in the air-gap (open-circuit condition) obtained from FEM and RN M5 ($y = h_{mbi} + h_m + e/4$).
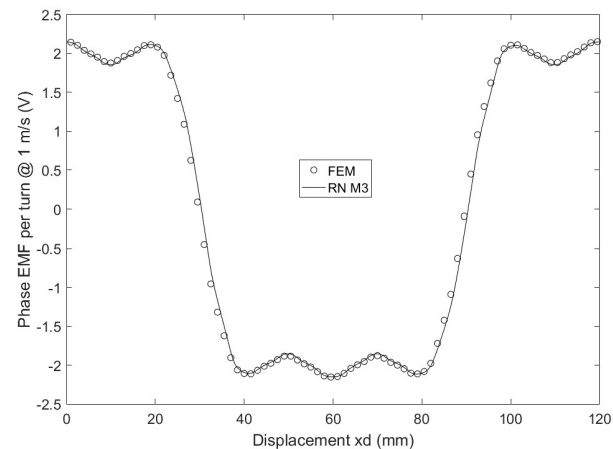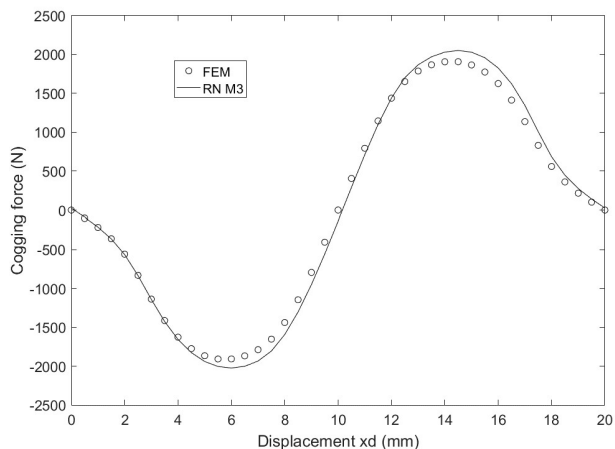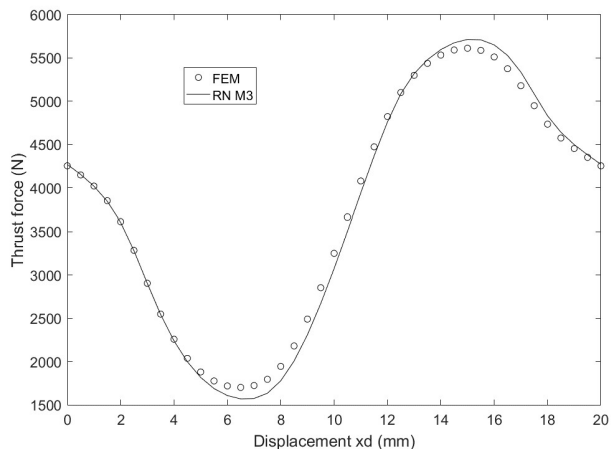

Fig. 21. Comparison of EMF waveforms for a linear speed $v = 1$ m/s.

obtained from the FEM. The match is not as good as what was obtained for the mesh scheme M1 [1], but it is good enough to consider the use of triangular element of interest.

Of course the use of triangular reluctance elements should be dedicated to regions which shapes and physics properties implies an impossibility to use other types of elements.

For example, the curved tooth tips of electrical machines can be difficult to be meshed using other types of reluctance elements; the use of triangular elements may become necessary.

For this first structure, the mesh scheme using exclusively the rectangular (square) elements (M1) is the one giving the best results as compared to FEM model because its geometric and physics properties are well adapted for such elements.

Nevertheless, the use of triangular elements for the stator didn't result in too high deviation as compared to FEM results, as it has been observed from results obtained using models RN M3 and RN M5.

(a) Cogging force

(b) Thrust force

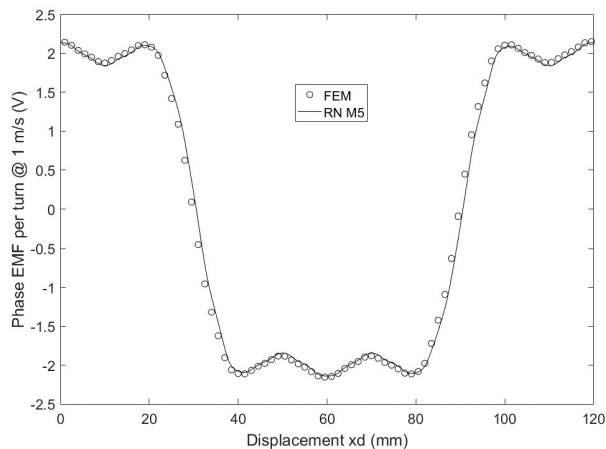Fig. 22. Comparison of force computation results obtained from FEM and RN M3.
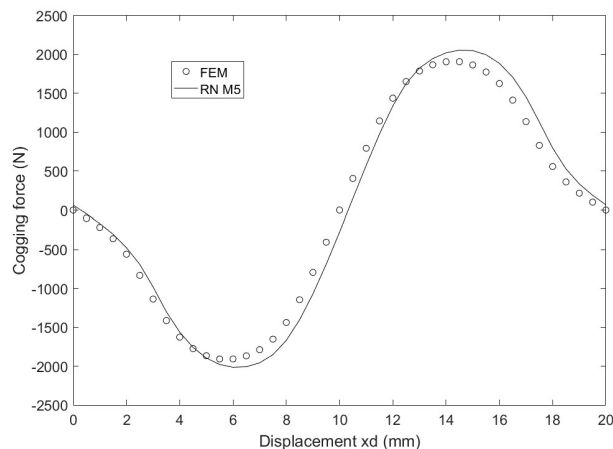

(a) Cogging force

(b) Thrust force

Fig. 24. Comparison of force computation results obtained from FEM and RN M5.

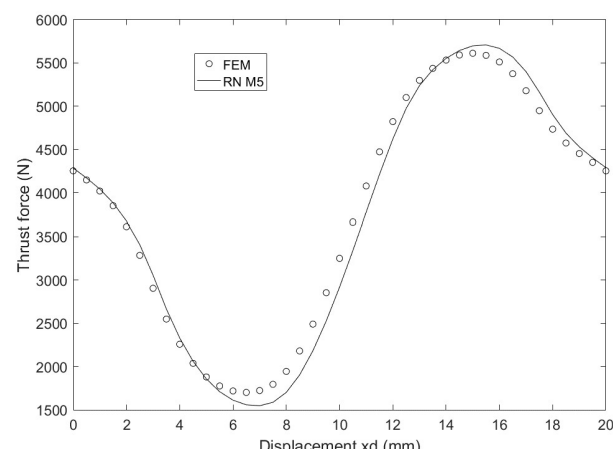Fig. 23. Comparison of EMF waveforms for a linear speed $v = 1$ m/s.

B.   Second Example

In order to further illustrate the use of triangular elements, a second example is treated in this subsection. Fig. 25 shows the studied structure.

Fig. 25(a) gives the geometric dimensions of the structure, which is supposed to be 1 m long in the third dimension (z direction). It contains two iron cores, in blue color, a permanent magnet, in red color, and an air-gap. This structure contains a geometric form, oblique frontier between the air and the upper

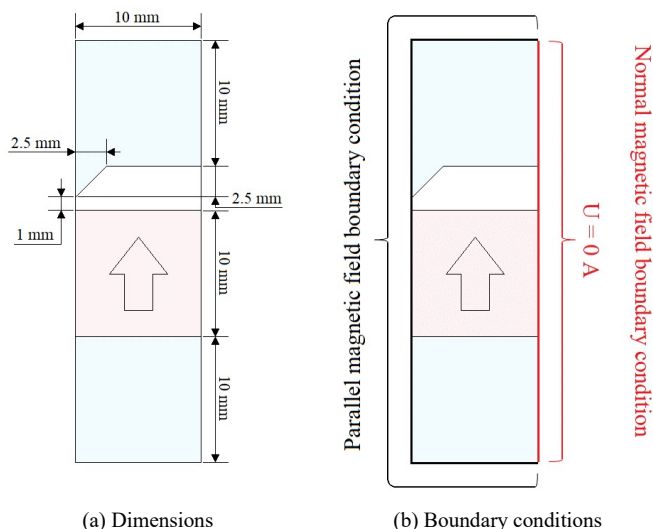(a) Dimensions   (b) Boundary conditions

Fig. 25. Second studied structure.

iron core, for which the use of triangular elements may be more convenient as compared to rectangular elements. Fig. 25(b) shows applied boundary conditions.

Two mesh schemes are compared for the modeling of this structure. They are illustrated by Fig. 26. This figure only shows the useful region where triangular elements are used Fig.

26(b). The rest of the structure is meshed with rectangular elements. Thus, the first mesh scheme M7 is based solely on rectangular elements. Rectangular elements, used to model the oblique frontier between the air and the upper iron core, are presented by Fig. 27. This technique has been successfully used in a previous reference [16].

This rectangular element (Fig. 27) can be regarded as the combination of two triangular elements with two reluctances each. A discussion on the different types of triangular reluctance elements is presented in following section.

For the mesh scheme M8, the rectangular elements of mesh scheme M7 located at the oblique frontier Fig. 26(a) are replaced by triangular elements Fig. 26(b).
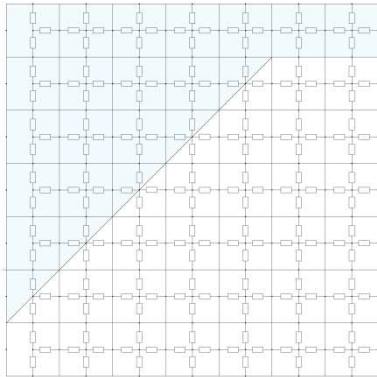
(a) Mesh scheme M7 (rectangular elements)
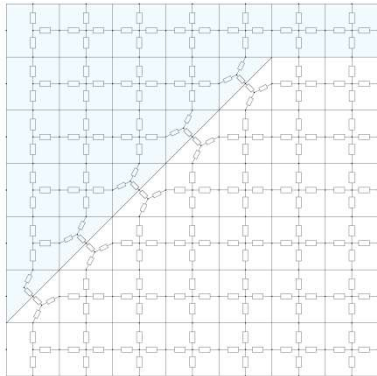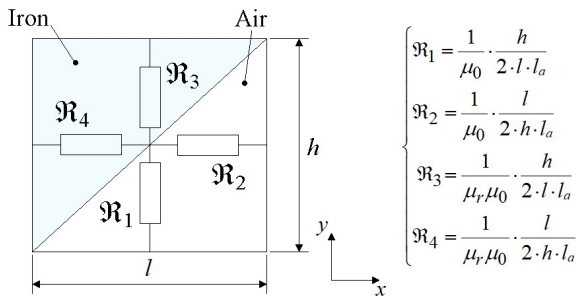

(b) Mesh scheme M8

Fig. 26. Compared meshes schemes.

Fig. 27. Rectangular reluctance elements used to model the oblique frontier.

$$\mathfrak{R}_1 = \frac{1}{\mu_0} \cdot \frac{h}{2 \cdot l \cdot l_a}$$
$$\mathfrak{R}_2 = \frac{1}{\mu_0} \cdot \frac{l}{2 \cdot h \cdot l_a}$$
$$\mathfrak{R}_3 = \frac{1}{\mu_r \mu_0} \cdot \frac{h}{2 \cdot l \cdot l_a}$$
$$\mathfrak{R}_4 = \frac{1}{\mu_r \mu_0} \cdot \frac{l}{2 \cdot h \cdot l_a}$$

The comparison study is done by drawing the magnetic flux density components waveforms obtained from both mesh schemes, and a finite element model. The components are obtained for two paths defined within the studied structure. Fig. 28 shows the two paths for which the comparison study is conducted.

Fig. 29(b) shows the flux lines obtained from the finite elements model. Fig. 30 compares the magnetic flux density components obtained from the two mesh schemes with those obtained from a finite element model for the first path (Path 1). Fig. 31 shows comparisons for the second path (Path 2).

At this stage, it should be noticed that the significant error in the magnetic field components obtained from the model based on the mesh scheme M7, is not due to a significant error in the computation of the mesh fluxes, but rather on the method used to compute the magnetic flux density components [1]. Indeed, at the frontier between two regions with different materials, there is a jump in the tangential magnetic flux density **B** Fig. 29(b), or the normal magnetic field **H**, which is a source of errors (numerical noise) even in the finite elements method, particularly in linear case. Knowing that the mesh of the MBGRN approach is not as fine as the finite element method Fig. 29(a), computing the average value from components located at a certain distance from the border will result in significant errors.
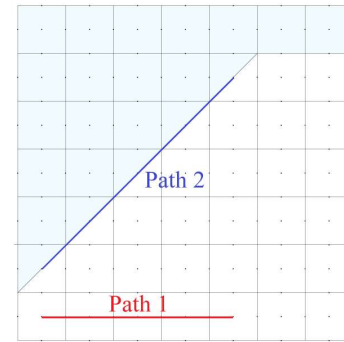

Fig. 28. Paths for the comparison study.

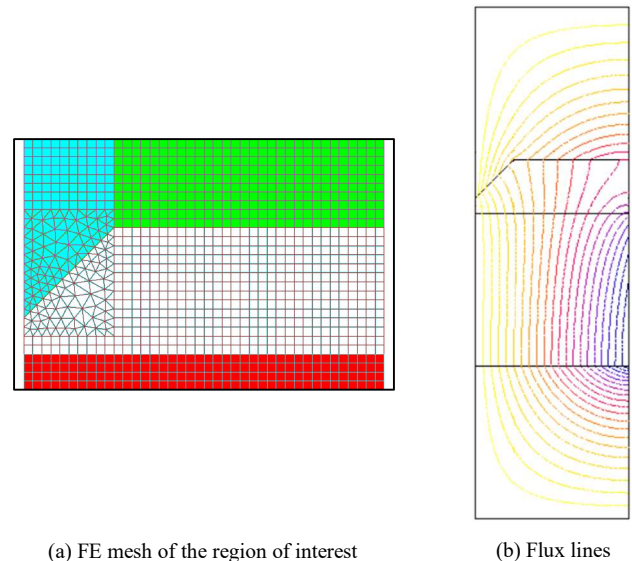(a) FE mesh of the region of interest   (b) Flux lines

Fig. 29. Flux lines obtained from the finite element model.

To avoid this problem, the magnetic flux density components, for mesh scheme M7, are recalculated as done for the mesh scheme M8. Fig. 32 illustrates how this is done for both schemes. It is advised to use this alternative approach whenever an oblique frontier is present.

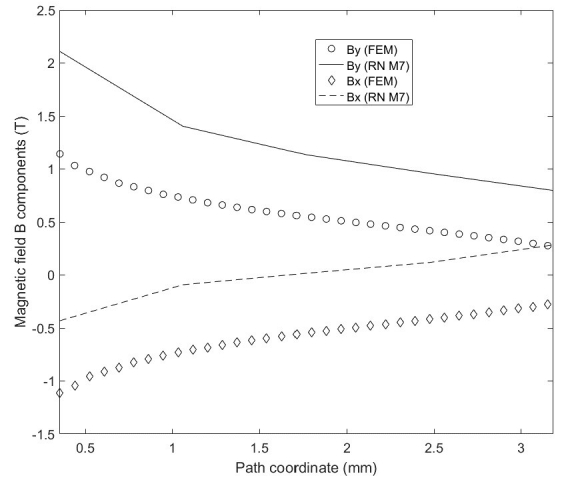(a) Comparison for mesh scheme M7
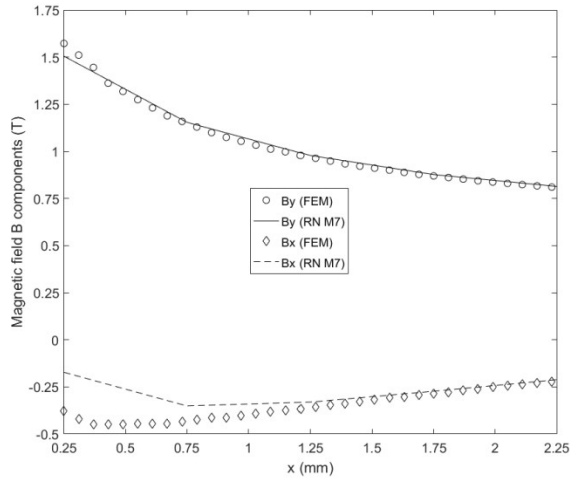
(a) Comparison for mesh scheme M7
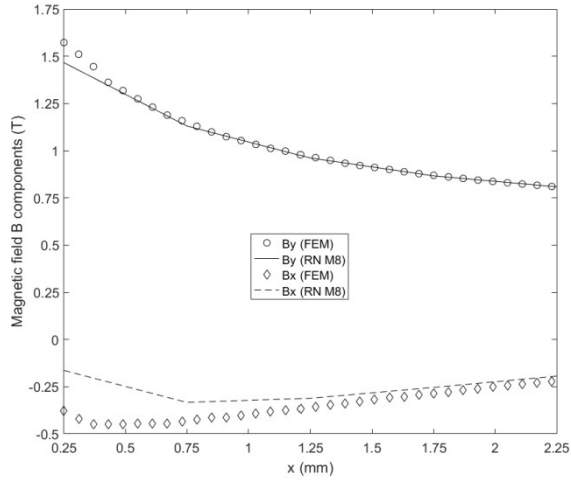
(b) Comparison for mesh scheme M8

Fig. 30. Comparison of magnetic flux density components for "Path 1".

(b) Comparison for mesh scheme M8

Fig. 31. Comparison of magnetic flux density components for "Path 2".

The magnetic flux density components are then compared again (Fig. 33), and as can be seen, the error in the results from mesh scheme M7 reduced drastically. Path coordinate, in Figs. 31 and 33, corresponds to the distance from the origin which is located at the left hand side bottom corner of the oblique border between the air and the upper iron core (Fig. 28).
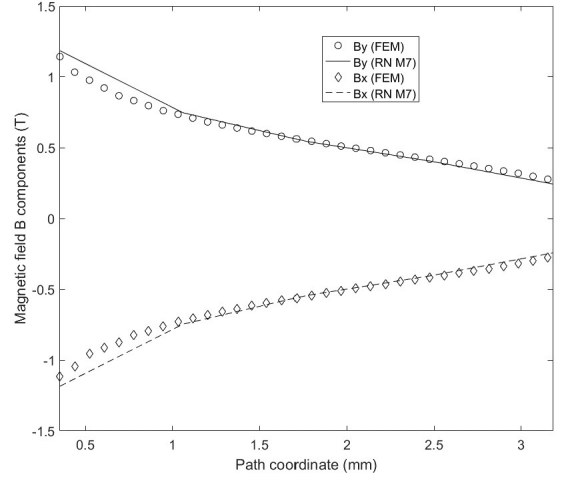
As compared to the finite element method, both mesh schemes gave relatively good results. The computation time for the mesh scheme M8 was consistently longer than the computation time of mesh scheme M7, even if the difference wasn't too significant, both taking few tens of milliseconds. It should be also noticed that the number of non-zero elements in the system matrix is higher for mesh scheme M8 (6436) as compared to mesh scheme M7 (6428). Programs coded under MATLAB environment allowing the analyses for this second structure can be downloaded from [17].

IV. ON THE USE OF ALTERNATIVE TRIANGULAR ELEMENTS

The triangular elements defined in section II.A are not the sole type of elements that can be selected when a triangular shape is adopted. Instead of using the barycenter of the triangle as the central node, the center of the inscribed circle, or the
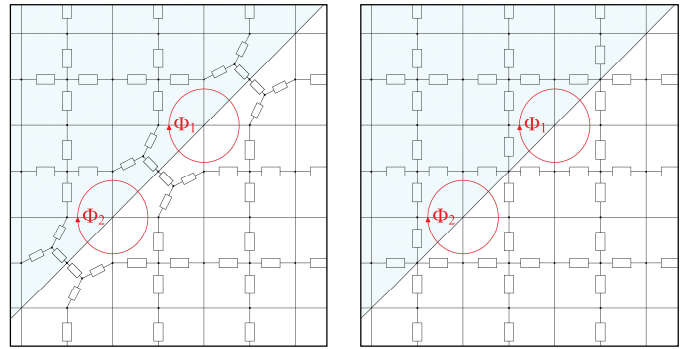

(a) Mesh scheme M8   (b) Mesh scheme M7
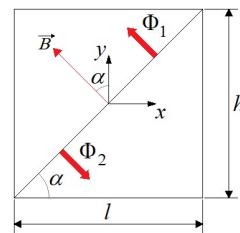
$$\begin{cases} B_x = \dfrac{-\left(\Phi_1 - \Phi_2\right)}{l_a\sqrt{l^2 + h^2}} \cdot \dfrac{h}{\sqrt{l^2 + h^2}} \\[4mm] B_y = \dfrac{\left(\Phi_1 - \Phi_2\right)}{l_a\sqrt{l^2 + h^2}} \cdot \dfrac{l}{\sqrt{l^2 + h^2}} \end{cases}$$

(c) Flux density components computation

Fig. 32. Computation of magnetic flux density components.
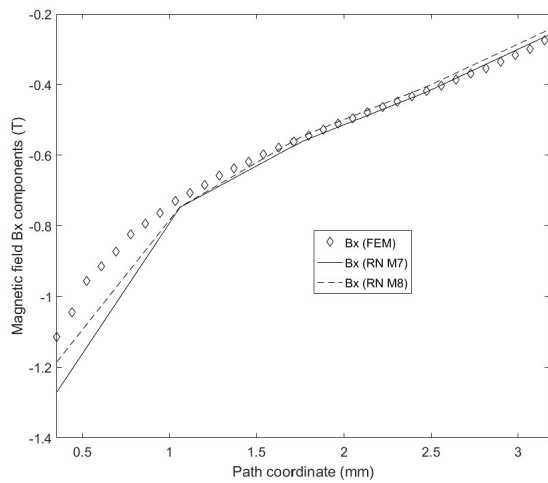
(a) Comparison of Bx components
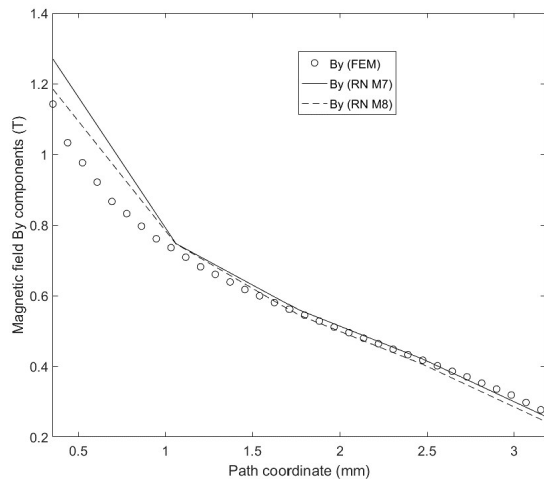
(b) Comparison of By components

Fig. 33. Comparison of magnetic flux density components for "Path 2".

circumscribed circle, can be used. Two other types can then be defined. They are defined in following subsections and used for the modeling of the second structure, studied in section III.B.

A. Inscribed Circle Center as Central Node

Fig. 34 shows an example of an element where the central node is the center of the inscribed circle. This center is obtained by drawing the bisectors of the three angles of the triangle, which are concurrent at this point. This point is always located inside the triangle.

The computation of the three reluctances $\mathcal{R}_1$, $\mathcal{R}_2$ and $\mathcal{R}_3$ is done as for the previous triangular element, defined in section II.A. Three trapezoids can be defined, each being related to one edge of the triangle. To draw a trapezoid, the parallel to the edge crossing the central node is first defined.

The trapezoid is constituted by four points corresponding to the two extreme points of the specific edge, and the two points corresponding to the intersection of the parallel line to this edge, and passing through the central node, with the two other edges of the triangle.

The reluctances of the trapezoids are computed considering a flux tube perpendicular to the bases of these trapezoids, as previously. More details are provided in the Appendix.
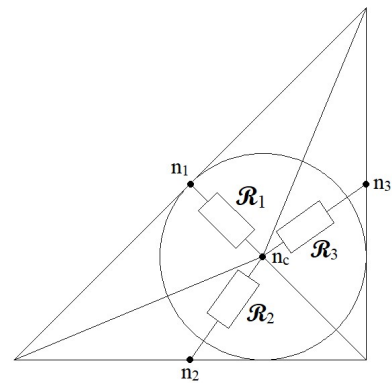

Fig. 34. Triangular reluctance element with the central node being the center of the inscribed circle.

B. Circumscribed Circle Center as Central Node

Fig. 35 shows an example of an element where the central node is the center of the circumscribed circle. This center is obtained by drawing the bisectors of the three edges of the triangle, which are concurrent at this point. This point is located inside the triangle if the triangle angles are all acute angles. It is located outside the triangle, if any of the angles is obtuse. If the triangle is a right-angled triangle, this center is located in the middle of the edge facing the right angle (midpoint of the hypotenuse) (Fig. 35).

In order to define the reluctances, which should be located inside the triangle, it is mandatory to avoid the use of obtuse triangles.

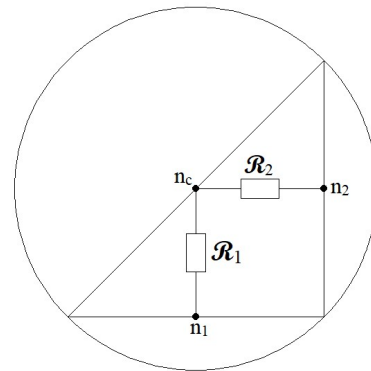The computation of the reluctances is done similarly to what has been described previously.

Fig. 35. Triangular reluctance element with the central node being the center of the circumscribed circle.
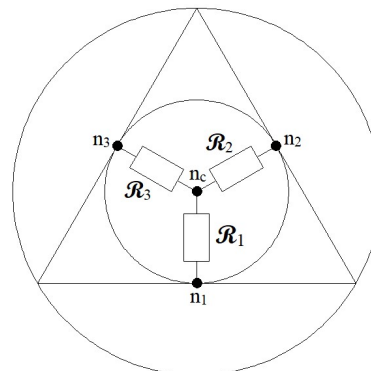

Fig. 36. Reluctance element in the case of an equilateral triangle ($\mathcal{R}_1 = \mathcal{R}_2 = \mathcal{R}_3$).

It should be noticed that for the equilateral triangles, the three types of triangular elements are equivalent. In this case, the barycenter coincides with the centers of the inscribed and circumscribed circles. Fig. 36 shows such an element.

C. Comparison of the Different Triangular Elements Types

In this section, the different triangular elements are used for the modeling of the structure studied in section III.B. The results obtained using the different meshes schemes including these triangular elements are compared to those issued from the rectangular mesh scheme and the FEM.

Figs. 37(a) and 37(b) compare the results from the different models for the x and y components of the magnetic flux density, respectively, for the first path "Path 1". Meshes schemes M9 and M10 correspond to meshes where the previous triangular elements are replaced by triangular elements with a central node being the center of inscribed and circumscribed circles, respectively.

Figs. 38(a) and 38(b) compare the results from the different models for the x and y components of the magnetic flux density, respectively, for the second path "Path 2".

As can be seen, all meshes schemes gave roughly good results. Even the rectangular elements scheme M7 gave good results, thanks to the adaptation of the elements located at the oblique frontier (Fig. 27). In fact these elements should be regarded as the combination of two triangular elements.

The general rule which can be drawn is to use the reluctance elements which allow respecting at most the geometric and physics properties and symmetries of modeled devices. The use of different types of elements, as has been done in this contribution, can constitute an alternative.

These are encouraging results which pushes toward the continuation of the research efforts on the MBGRN approach. Readers interested by deepening the study of MBGRN are invited to download the MATLAB programs provided through the links [14] [17].

V. CONCLUSIONS

An introduction to the MBGRN approach using triangular elements has been presented. It has been observed that the mesh should be based on reluctance elements which allow respecting at most the geometric and physics properties and symmetries of modeled devices. The triangular elements should be used in regions where the use of rectangular elements is not possible, as for example oblique frontiers.

The provided programs have been coded under MATLAB environment. Very simple instructions have been used to make them the most simple to understand.
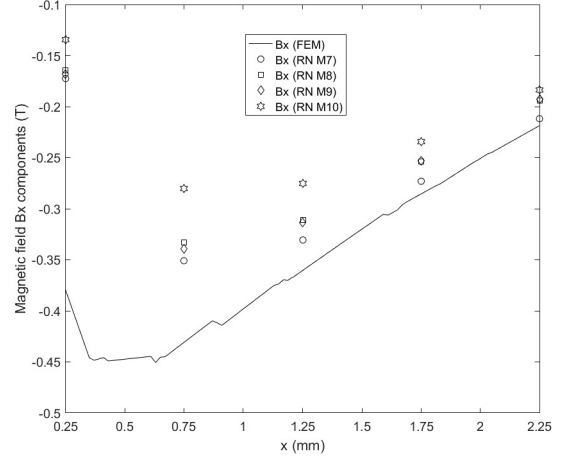
Along with this contribution, these programs can help the readers to deepen their knowledge of the MBGRN approach.

The main goal of this contribution is to introduce the MBGRN approach using triangular elements. It is a part of a wider project aiming at defining a modeling framework based on MBGRN with a good "accuracy/computation time" ratio.
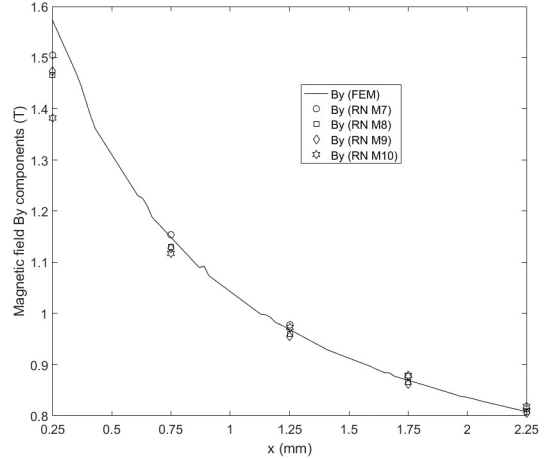
APPENDIX

Fig. 39 illustrates how the reluctance expression is computed for a trapezoidal element. Following mathematical development details how the expression given by eq. (2) is obtained:

$$
\begin{aligned}
\mathcal{R}_1 &= \int_0^h \frac{1}{\mu_r \mu_0 w(y) l_a} dy = \int_0^h \frac{1}{\mu_r \mu_0 \left(w_1 + \dfrac{(w_2 - w_1)}{h} y \right) l_a} dy \\
&= \frac{1}{\mu_0 \mu_r} \frac{h}{l_a (w_2 - w_1)} \left[\ln \left(w_1 + \frac{(w_2 - w_1)}{h} y \right) \right]_0^h \\
&= \frac{1}{\mu_0 \mu_r} \frac{h \ln(w_2 / w_1)}{l_a (w_2 - w_1)}
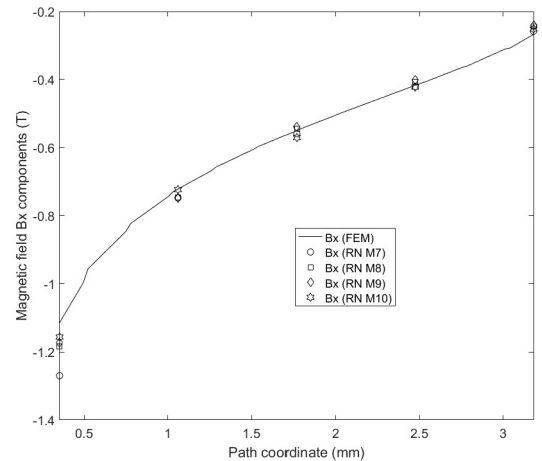\end{aligned} \tag{A.1}
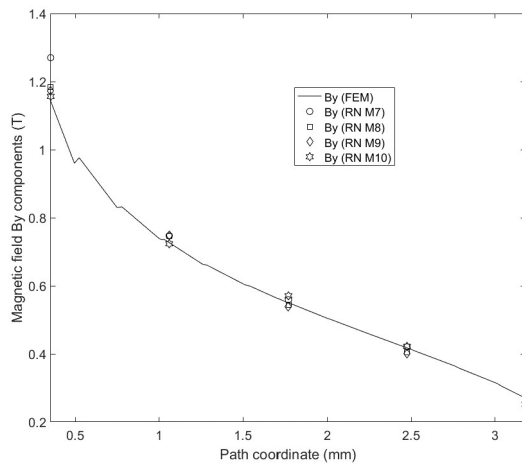$$

(a) Comparison of Bx components

(b) Comparison of By components

Fig. 37. Comparison of magnetic flux density components for "Path 1".

(a) Comparison of Bx components

(b) Comparison of B*y* components

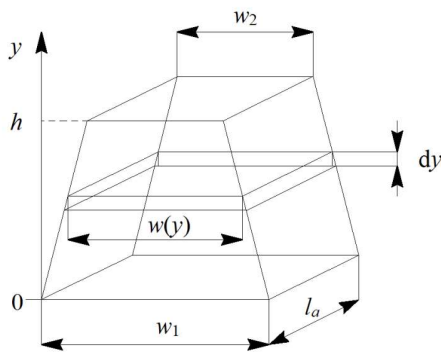Fig. 38. Comparison of magnetic flux density components for "Path 2".

Fig. 39. Reluctance computation for a trapezoidal flux tube.

REFERENCES

[1] S. Yang, S. Asfirane, S. Hlioui, S. Mezani, G. Krebs, Y. Amara, G. Barakat, M. Gabsi, and W. Hua,, "Introduction to mesh based generated lumped parameter models for electromagnetic problems," *CES Transactions on Electrical Machines and Systems*, vol. 5, no. 2, pp. 152–162, June 2021. DOI: 10.30941/CESTEMS.2021.00019.

[2] K. J. W. Pluk, J. W. Jansen, and E. A. Lomonova, "3-D hybrid analytical modeling: 3-D Fourier modeling combined with mesh-based 3-D magnetic equivalent circuits," *IEEE Trans. Magn.*, vol. 51, no. 12, paper 8208614, Dec. 2015. DOI: 10.1109/TMAG.2015.2455951

[3] K. J. W. Pluk, J. W. Jansen, and E. A. Lomonova, "Hybrid analytical modeling: Fourier modeling combined with mesh-based magnetic equivalent circuits," *IEEE Trans. Magn.*, vol. 51, no. 8, paper 8106812, August 2015. DOI: 10.1109/TMAG.2015.2419197

[4] M. Amrhein and P. T. Krein, "3-D magnetic equivalent circuit framework for modeling electromechanical devices," *IEEE Trans. Energy Convers.*, vol. 24, no. 2, pp. 397–405, Jun. 2009. DOI: 10.1109/TEC.2009.2016134

[5] H. Gholizadi, M. Mirsalim, and M. Mirzaei, "An improved equivalent magnetic circuit network method for consideration of motional eddy currents in a solid conductor," *Amirkabir Journal of Science and Research*, vol. 37, no. 2, pp. 63–68, 2007.

[6] Y. H. Kim, C. S. Jin, S. Kim, Y. D. Chun, and J. Lee, "Analysis of hybrid stepping motor using 3D equivalent magnetic circuit network method based on trapezoidal element," *J. Appl. Phys.*, vol. 91, no. 10, pp. 8311–8313, 2002. https://doi.org/10.1063/1.1456046.

[7] J. Hur, I.-S. Jung, and D.-S. Hyun, "Lateral characteristic analysis of PMLSM considering overhang effect by 3 dimensional equivalent magnetic circuit network method," *IEEE Trans. Magn.*, vol. 34, no. 5, pp. 3528–3531, Sep. 1998. DOI: 10.1109/20.717832

[8] S. Asfirane, S. Hlioui, Y. Amara, and M. Gabsi, "Study of a Hybrid Excitation Synchronous Machine: Modeling and Experimental

Validation," Mathematical and Computational Applications, vol. 24, no. 2, p. 34, Mar. 2019. doi: 10.3390/mca24020034.

[9] A. Demenko, J. K. Sykulski, and R. Wojciechowski, "On the equivalence of finite element and finite integration formulations," *IEEE Trans. Magn.*, vol. 46, no. 8, pp. 3169–3172, Aug. 2010. DOI: 10.1109/TMAG.2010.2043506

[10] C. J. Carpenter, "Finite-element network models and their application to eddy-current problems," Proc. Inst. Elect. Eng., vol. 122, no. 4, pp. 455–462, Apr. 1975. DOI: 10.1049/piee.1975.0125.

[11] H. W. Derbas, J. M. Williams, A. C. Koenig, and S. D. Pekarek, "A comparison of nodal- and mesh-based magnetic equivalent circuit models, ," *IEEE Trans. Energy Convers.*, vol. 24, no. 2, pp. 388–396, Jun. 2009. DOI: 10.1109/TEC.2008.2002037

[12] G. Meunier, *The Finite Element Method for Electromagnetic Modeling*, London, U.K.: ISTE Ltd., 2008. [Online]. Available: http://www.iste.co.uk/book.php?id=168

[13] V. Ostovic, *Dynamics of Saturated Electric Machines*, Springer-Verlag New York Inc., 1989.

[14] https://1drv.ms/u/s!AogSAGtYvycUl01gsWPvbZWJhyNJ?e=Caw1mZ

[15] A. Foggia, J.-L. Coulomb, G. Reyne, F. Ossart, and A. Kedous-Lebouc, "The French experience in integrating the program FLUX2D in the undergraduate curriculum at the Institut National Polytechnique de Grenoble," *IEEE Trans. Educ.*, vol. 36, no. 2, pp. 85–93, May 1993. DOI: 10.1109/13.214713.

[16] S. Ouagued, Y. Amara and G. Barakat, "Cogging force analysis of linear permanent magnet machines using a hybrid analytical model," *IEEE Trans. Magn.*, vol. 52, no. 7, paper 8202704, July 2016. DOI: 10.1109/TMAG.2016.2521825

[17] https://1drv.ms/u/s!AogSAGtYvycUm05i-5S5D9BQSwNe?e=IAryn3

Haidar Y. Diab received the M.Sc. degree in Electrical and Electronics Engineering from the Lebanese University, Faculty of Engineering, Lebanon in 2019. In 2022, he acquired the Ph.D. degree from Université Le Havre Normandie, France. He is currently a postdoctoral researcher with the "Groupe de Recherche en Electrotechnique et Automatique du Havre" (GREAH), France. His research interests include the design and modeling of electric machines and magnetic gears for renewable energy applications.
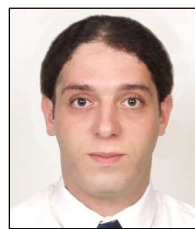
Salim Asfirane received the Ingénieur d'État degree in electrical engineering from École Nationale Polytechnique in Algiers, Algeria and the M.Sc. degree in electrical engineering from École Normale Supérieure de Cachan, France, in 2014 and 2015 respectively. In 2019, he finished his Ph. D. studies in Electrical Engeneering in Laboratoire des Systémes et Applications des Technologies de l'Information et de l'Énergie (SATIE Laboratory) in collaboration with Groupe de Recherche en Électrotechnique et Automatique du Havre (GREAH Laboratory) where he is currently pursuing his research. His interests include electromagnetic modeling methods and innovative design topologies of rotating and linear electrical machines.

Nicolas Bracikowski received the B.Sc. and M.Sc. degrees in electrical engineering from the University of Artois (France). He received his Ph.D. degree from Ecole Centrale de Lille (France), in 2012. Since 2013, he is an Associate Professor at Nantes University (France), where he carries out research in IREENA Laboratory (Institut de Recherche en Energie Electrique de Nantes Atlantique). His area research includes: optimal design of electrotechnical device, multi-physics lumped models and acoustic noise in electrical machine.

Frédéric Gillon obtained an Engineer Diploma in 1992 and a Ph.D. in 1997 at Université des Sciences et Technologies de Lille. He is currently Associate Professor at Ecole Centrale de Lille since 1999. His research subjects are the design by optimization of electric systems and electrical machines for traction applications or renewable energy production.

Yacine Amara (S'00–M'03–SM'18) received the Electrical Engineering Degree from Ecole Nationale Polytechnique d'Alger, El-Harrach, Algeria, in 1997, and the Ph.D. degree from the University of Paris XI, Orsay, France, in 2001. He is currently with the Groupe de Recherche en Electrotechnique et Automatique du Havre (GREAH), University of Le Havre, Le Havre, France, where he holds a Full Professor position, and is heading the Electrical Machines and Actuators thematic. His research interests include the design, modeling, and control of rotating and linear permanent-magnet machines for automotive and renewable energies applications.